Numerical Heat Transfer, Part A, 68: 548–565, 2015

ISSN: 1040-7782 print/1521-0634 online
DOI: 10.1080/10407782.2014.986397

Taylor & Francis
Taylor & Francis Group

NUMERICAL INVESTIGATION OF NANOFLUID FLOW AND HEAT TRANSFER AROUND A CALABASH-SHAPED BODY

Shuangling Dong, Bingyang Cao, and Zengyuan Guo
Department of Engineering Mechanics, Tsinghua University, Beijing, China

Numerical simulation on unsteady flow and heat transfer of alumina–water nanofluids around a calabash-shaped body was performed in the present study. Improved models of drag force and Brownian force were introduced. As the reaction time of the particle perturbation is short, fluctuation in vorticity is more intense than that in temperature, and many extreme values are found. The streamline is uplifted near the separation point due to the contribution of the particle inertia, which increases the recirculation zone of the quasi-steady vortex. Fewer particles enter the vortex near the waist portion from the separation region, and relatively more particles enter the recirculation region from the reattachment zone. The local streamline is straightened and flow heat transfer is enhanced. It is shown that the variation in the Nusselt number is strongly related to the critical points along the wall.

1. INTRODUCTION

As a new generation of highly efficient heat transfer media, nanofluids, which are colloidal suspensions containing nanoscale particles, have potential applications in aerospace and biomedical engineering among other fields. Additives in nanofluids mainly include metal nanoparticles, nonmetallic nanoparticles, carbon nanotubes, and nanodroplets. The base liquid is water, alcohol, oil, or other heat transfer fluids commonly used. When appropriate amounts of metal oxide nanoparticles of high thermal conductivity are added to the base fluid, the thermal conductivity of the mixture is increased and the heat transfer performance will be improved. Lee et al. [1] studied the thermal conductivity characteristics of nanofluids and analyzed the differences between the experimental data and theoretical models. Wang et al. [2] reviewed the main potential mechanisms contributing to the thermal conductivity enhancement of nanofluids reported in previous studies. Based on their experimental data, it was concluded that the key factor increasing the thermal conductivity is nanoparticle aggregation. Mahian et al. [3] focused on the applications of nanofluids in solar energy conversion and analyzed the performance of solar equipment.

Received 7 August 2014; accepted 7 November 2014.

Address correspondence to Bingyang Cao, Department of Engineering Mechanics, Tsinghua University, 100084, Beijing, China. E-mail: caoby@tsinghua.edu.cn

Color versions of one or more of the figures in the article can be found online at www.tandfonline.com/unht.

NOMENCLATURE

c_p	specific heat, J/(kg · K)	x,y	coordinates, m
D	diameter of the small major arc, m	α	thermal diffusivity, m^2/s
d_p	diameter of nanoparticle, m	μ	dynamic viscosity, kg/(m · s)
k	thermal conductivity, W/(m · K)	ν	kinematic viscosity, m^2/s
k_B	Boltzmann constant	ρ	density, kg/m^3
Kn	Knudsen number	ϕ	nanoparticle volume fraction
m	mass, kg	ω	vorticity, 1/s
Nu	local Nusselt number	**Superscripts**	
p	pressure, Pa	*	dimensionless
Pr	Prandtl number	**Subscripts**	
Re	Reynolds number	∞	in free stream
St	Strouhal number	f	base fluid
t	time, s	p	nanoparticle
T	temperature, K	w	at the wall
u,v	velocity, m/s		

Over the past few years, numerous experiments and numerical simulations have been performed on nanofluid flow [4–6]. Many researchers have simulated nanofluid heat transfer inside enclosures of various shapes, including natural convection in square [7], triangle [8], and U-shaped cavities [9]. For convective outflows, Zhang et al. [10] simulated the convective heat transfer around a circular cylinder using the immersed boundary method. Valipour and Ghadi [11] analyzed the steady nanofluid flow around a cylinder at low Reynolds number. It was observed that the pressure coefficient along the cylinder wall increased in the region with adverse pressure gradient while the recirculation length was increased with the addition of nanoparticles. In the case of unsteady flow around a circular cylinder, Sarkar et al. [12] conducted a numerical simulation. It was shown that the presence of nanoparticles played a role in balancing the buoyancy force, which reduced its impact and stabilized the flow. Etminan-Farooji et al. [13] studied the heat transfer process around a square cylinder numerically, indicating an optimum volumetric ratio for enhanced heat transfer performance. However, the flow model they used in the above simulations was of single phase and thus the interaction between particles and fluid could not be reflected precisely, especially in the presence of unsteady vortices.

Various geometries of blunt bodies exist in related practical applications, some being distinct from the circular or square cylinder. Specifically, metallic high thermal conductivity inserts and the longitudinally adjustable tubes for heating radiators can be considered as calabash shaped. In the present investigation, we study the heat transfer process around the calabash-shaped body developed. Theoretically, the flow and heat transfer around the blunt body involve both steady vortex pairing and unsteady vortex shedding, which interacts with the mainstream demonstrating the complex flow processes. A discrete-phase model is adopted to simulate the nanofluid flow around the newly shaped body. Improved models of Brownian force and drag force were used in the numerical computation. The evolution of nanoparticles near the waist portion and in the near wake is examined in particular. The heat transfer performance of nanofluids around the body was also analyzed.

2. GOVERNING EQUATIONS

In the present study, a discrete-phase model is used to simulate the nanofluid flow with particles, computed by the Lagrange method. For the continuous fluid phase, the flow and heat transfer processes are determined by the conservation laws of mass, momentum, and energy. The flow of water can be considered to be incompressible, and the governing equations are expressed in vector form as follows [14].

The continuity equation is written as

$$\nabla \cdot \overrightarrow{V} = 0. \tag{1}$$

The momentum equation is given by

$$\frac{\partial \overrightarrow{V}}{\partial t} + (\overrightarrow{V} \cdot \nabla)\overrightarrow{V} = \frac{1}{\rho}\left(-\nabla p + \mu \nabla^2 \overrightarrow{V}\right) + \overrightarrow{F_{\mathrm{p}}}. \tag{2}$$

The energy equation can be expressed as

$$\frac{\partial T}{\partial t} + \overrightarrow{V} \cdot \nabla T = \frac{1}{(\rho c_{\mathrm{p}})} \nabla \cdot (k \nabla T) + q_{\mathrm{p}}. \tag{3}$$

The source terms $\overrightarrow{F_{\mathrm{p}}}$ and q_{p} represent the two-way coupling of momentum and energy, respectively, between the fluid and nanoparticles. These are given by the following expression [15]:

$$\overrightarrow{F_{\mathrm{p}}} = \frac{1}{\rho} \sum_{n_{\mathrm{p}}} \frac{m_{\mathrm{p}}}{\delta V} \frac{d\overrightarrow{V_{\mathrm{p}}}}{dt}, q_{\mathrm{p}} = \frac{1}{\rho} \sum_{n_{\mathrm{p}}} \frac{m_{\mathrm{p}}}{\delta V} c_{\mathrm{pp}} \frac{dT_{\mathrm{p}}}{dt}, \tag{4}$$

where δV is the cell volume, n_{p} represents the number of particles within the cell, m_{p} is the mass, and T_{p} is the temperature of the nanoparticles. $\frac{d\overrightarrow{V_{\mathrm{p}}}}{dt}$ and $\frac{dT_{\mathrm{p}}}{dt}$ denote the rates of change for velocity and temperature of particles, respectively.

The following variables are defined before simulating the process:

$$\begin{aligned} x^* &= \frac{x}{D}, y^* = \frac{y}{D}, u^* = \frac{u}{U_\infty}, v^* = \frac{v}{U_\infty}, \\ t^* &= \frac{U_\infty t}{D}, p^* = \frac{p}{\rho {U_\infty}^2}, \rho^* = \frac{\rho}{\rho_\infty}, T^* = \frac{T - T_\infty}{T_w - T_\infty}, \end{aligned} \tag{5}$$

Equations (1)–(3) can then be rewritten in dimensionless form as below.

The continuity equation is given by

$$\nabla \cdot \overrightarrow{V}^* = 0. \tag{6}$$

The momentum equation can be expressed as

$$\frac{\partial \overrightarrow{V}^*}{\partial t^*} + (\overrightarrow{V}^* \cdot \nabla)\overrightarrow{V}^* = -\nabla p^* + \frac{1}{\mathrm{Re}}\nabla^2 \overrightarrow{V}^* + \overrightarrow{F_\mathrm{p}}^*. \tag{7}$$

The energy equation is written as

$$\frac{\partial T^*}{\partial t^*} + \overrightarrow{V}^* \cdot \nabla T^* = \frac{1}{\mathrm{Re}\,\mathrm{Pr}}\nabla^2 T^* + q_\mathrm{p}{}^*. \tag{8}$$

where $\mathrm{Re} = \frac{\rho U_\infty D}{\mu}$, $\mathrm{Pr} = \frac{\nu}{\alpha}$, $\alpha = \frac{k}{\rho c_\mathrm{p}}$, in which ν_f and α_f represent the kinematic viscosity and the thermal diffusion coefficients of the fluid respectively. The physical properties of alumina–water nanofluids at reference temperature are shown in Table 1 [16].

In the Lagrangian coordinate, the motion of nanoparticles is governed by

$$\frac{d\overrightarrow{V_\mathrm{p}}}{dt} = \overrightarrow{F_\mathrm{D}} + \overrightarrow{F_\mathrm{B}} + \overrightarrow{F_\mathrm{T}} + \overrightarrow{F_\mathrm{L}}. \tag{9}$$

The terms on the right-hand side of the equation represent the drag force, the Brownian force, the thermophoretic force, and the Saffman's lift force on the particles. In previous numerical simulations, the drag force $\overrightarrow{F_\mathrm{D}}$ exerted on the particles by the surrounding fluid was calculated by the Stokes drag equation [17]. Taking into account the multiparticle interactions and the special feature of a liquid layer absorbed by nanoparticles in the present study, the drag force is calculated by the improved expression proposed by Dong et al. [18], in which the viscosity is taken as $\mu_\mathrm{l}(\delta)$:

$$\overrightarrow{F_\mathrm{D}} = \sum_{n'} \overrightarrow{F_{\mathrm{D}'}}, \tag{10}$$

where n' represents the number of the particles contributing to the reference particle. The velocity is taken as the velocity difference between the particle and the fluid.

Due to the small size effect, another key force acting on nanoparticles in fluid is the Brownian force. The improved Brownian force model is adopted and its component is calculated by [19]:

$$\overrightarrow{F_\mathrm{B}} = \xi_i \sqrt{\frac{\pi \overline{S}}{\Delta t}}, \tag{11}$$

where ξ_i is the Gaussian random number with zero mean and unit variance, $\overline{S} = R_\mathrm{S}\frac{2k_\mathrm{B}T\beta}{m \times C_\mathrm{c}}$, in which R_S is the improvement coefficient, k_B denotes the Boltzmann constant, β represents the Stokes drag coefficient per unit mass, m^* is known as the effective mass, and C_c is the Cunningham correction factor.

Table 1. Thermophysical properties of fluid and nanoparticles

Base fluid/ nanoparticles	Density (kg/m^3)	Specific heat (J/(kg · K))	Thermal conductivity (W/(m · K))
Water	997.1	4,180	0.613
Al_2O_3	3,970	765	40

The thermophoretic force included in the movement equation of particles is given by [17]:

$$\overrightarrow{F_{\mathrm{T}}} = -\frac{6\pi d_{\mathrm{p}}\mu^2 C_s(K + C_{\mathrm{t}}Kn)}{\rho(1 + 3C_{\mathrm{m}}Kn)(1 + 2K + 2C_{\mathrm{t}}Kn)}\frac{1}{T}\nabla T, \tag{12}$$

where the thermally related coefficients $C_{\mathrm{s}} = 1.17$, $C_{\mathrm{t}} = 2.18$, $C_{\mathrm{m}} = 1.14$, and the ratio of thermal conductivity $K = k/k_{\mathrm{p}}$.

Saffman's lift force due to the contribution of the shear effect is calculated by [20]:

$$\overrightarrow{F_{\mathrm{L}}} = \frac{2K_{\mathrm{s}}\nu^{1/2}\rho d_{\mathrm{ij}}}{\rho_{\mathrm{p}} d_{\mathrm{p}}(d_{\mathrm{lk}}d_{\mathrm{kl}})^{1/4}}(\vec{V} - \overrightarrow{V_{\mathrm{p}}}), \tag{13}$$

where K_{s} is taken as 2.594 and d_{ij} is the deformation tensor.

The unsteady temperature equation for a particle can be expressed as [21]:

$$\frac{dT_{\mathrm{p}}}{dt} = \frac{6k\mathrm{Nu}_{\mathrm{p}}}{\rho_p c_{\mathrm{pp}} d_{\mathrm{p}}^2}(T - T_{\mathrm{p}}), \tag{14}$$

where Nu_{p} is the Nusselt number for nanoparticles, which is expressed as the Ranz–Marshall correlation:

$$\mathrm{Nu}_{\mathrm{p}} = 2 + 0.6\mathrm{Re}_{\mathrm{p}}^{1/2}\mathrm{Pr}^{1/3}, \tag{15}$$

where the particle Reynolds number $\mathrm{Re}_{\mathrm{p}} = \frac{\rho d_{\mathrm{p}}\left|\overrightarrow{V_{\mathrm{p}}} - \vec{V}\right|}{\mu}$.

Due to the unsteady and nonuniform distribution of nanoparticles, the effective thermal conductivity for local nanofluids changes constantly. To readily characterize the heat transfer performance of the fluid, the local Nusselt number can be obtained by

$$\mathrm{Nu} = -\left(\frac{\partial T}{\partial n}\right)\Big|_{\mathrm{w}}, \tag{16}$$

where n denotes the wall normal direction and the subscript w represents the value at the wall. According to the local Nusselt number, the average Nusselt number along the wall is calculated by

$$\overline{\mathrm{Nu}} = \frac{1}{S}\int_0^S \mathrm{Nu}dS, \tag{17}$$

where S is the arc length along the wall. The time-averaged Nusselt number can be expressed as

$$\overline{\overline{\mathrm{Nu}}} = \frac{1}{T_{\mathrm{c}}}\int_0^{T_{\mathrm{c}}} \overline{\mathrm{Nu}}dt, \tag{18}$$

where T_{c} is the time period of the flow past the calabash-shaped body.

3. BOUNDARY CONDITIONS AND NUMERICAL VALIDATION

The present simulation of nanofluids flow and heat transfer is performed based on a discrete-phase model. In the present study, the characteristic-based split algorithm [22] is used to simulate incompressible viscous flow around a calabash-shaped body with low Reynolds number. When calculating the momentum and energy equations, the source terms should be computed representing the coupling between the fluid and nanoparticles. The impact of nanoparticles on the fluid is reflected by the modified source terms in the Navier–Stokes equations. The behaviors of discrete particles are solved by the force and heat transfer balance equations.

Due to two-dimensional (2D) flow characteristics, the governing equations for the fluid flow are 2D unsteady N–S equations. The distribution of the elements around the wall is shown in Figure 1, in which the major arc portion of the larger

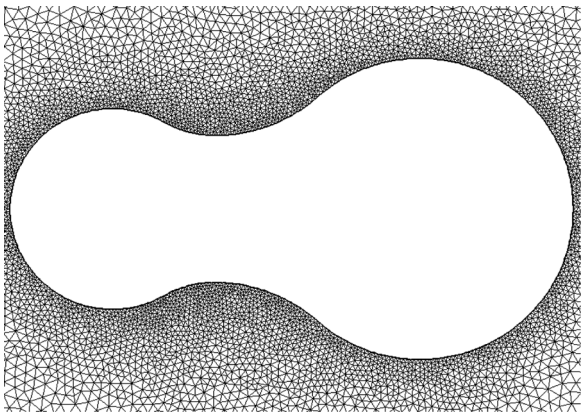

Figure 1. Elements distributed around the wall.

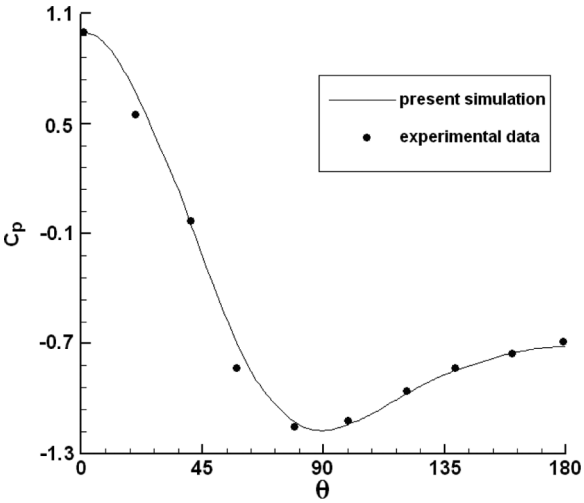

Figure 2. Comparison of the wall pressure coefficients.

Table 2. Effect of different numbers of elements and nodes on computation results

Mesh	Nodes	Elements	N_w	$\overline{\overline{Nu}}$
M1	11,329	22,046	266	8.026
M2	13,925	27,106	399	8.012
M3	16,374	31,866	539	8.008

circle is 1.5 times the diameter of the smaller circle. The computational domain of the present problem is a rectangle and the distribution of the elements around the cylinder is shown in this figure. The height of the region is 10 times the diameter of the small circle, while the length is 20 times the diameter and the region contains 27,106 triangular elements.

An undisturbed uniform free stream is assigned at the inlet. Alumina nanoparticles enter the domain at the same velocity and temperature. At the outlet boundary, the nonreflective boundary condition is applied which can eliminate the influence of the boundary on numerical results. As Kn <0.001 is valid for the problem, no-slip velocity and isothermal boundary conditions are prescribed at the walls.

For validation of the calculation, different wake flow regimes around a circular cylinder are selected as the typical bluff body to check the accuracy of the Fortran code. Figure 2 shows the wall pressure distribution of the steady vortex flow at $Re = 40$. Comparison of the results to the experimental data of Grove et al. [23]

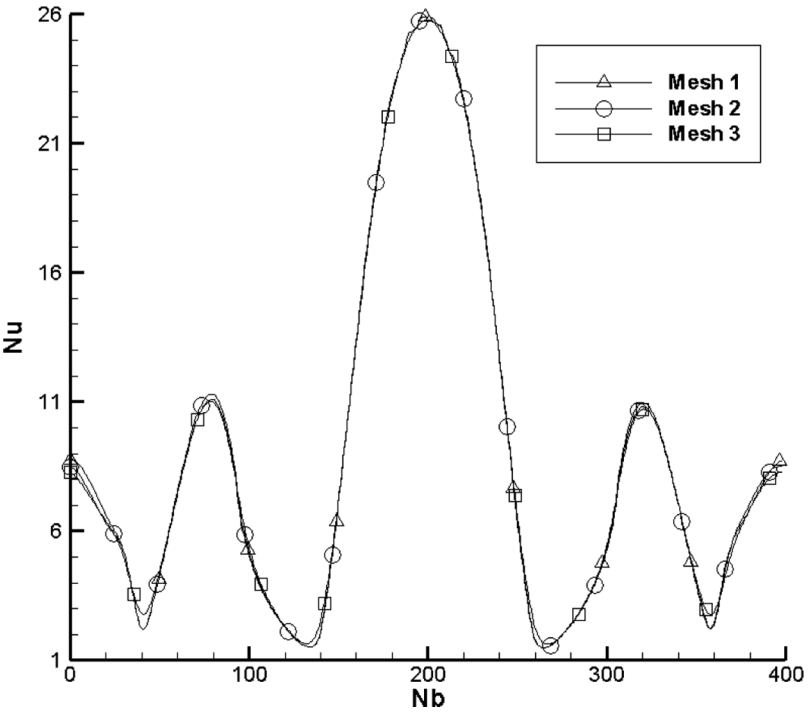

Figure 3. The Nusselt number distribution along the wall.

shows satisfactory agreement. For the unsteady vortex street ($\mathrm{Re} = 100$), the calculated result for St is 0.165, which is consistent with the value of 0.164 given by Williamson [24]. The average Nusselt number from the present computation is 5.07, the numerical value reported by Mettu is 5.08 [25], and the corresponding value from experimental investigation is 5.19 [26]. The present result thus shows satisfactory agreement with previous numerical and experimental results.

Unstructured nonuniform mesh is used for discretization, which is finer close to the wall where steep gradients are found in velocity and temperature fields. A grid-independence study is carried out using three different nonuniform meshes. The total numbers of nodes and finite elements used in this study are listed in Table 2, where N_w is the number of nodes over the wall.

The flow Reynolds number of 120 and the Prandtl number of 6.076 are prescribed in the computation with the average volume fraction of 0.01. The distribution of Nusselt number calculated is depicted in Figure 3, where N_b is the node number along the wall which starts at the trailing edge point. As shown in Table 2, the results for the second mesh are satisfactory, and further addition of mesh has little effect on improving the accuracy of simulation. Therefore, different results obtained in the present investigation are based on the second set of mesh.

4. RESULTS AND DISCUSSION

Figures 4*a* and 4*b* illustrate the simultaneous vorticity and temperature distribution, respectively, in the unsteady wake flow. It will be observed that the configuration of the two contours is very similar in the downstream wake, which is consistent with that in the cylinder wake. There also exists some difference in the near wake, which is due to the nonuniform distribution of vorticity along the wall and the constant temperature condition. In fact, the 2D vorticity equation for incompressible flow is $\frac{\partial \omega}{\partial t} + u\frac{\partial \omega}{\partial x} + v\frac{\partial \omega}{\partial y} = \nu\left(\frac{\partial^2 \omega}{\partial x^2} + \frac{\partial^2 \omega}{\partial y^2}\right)$, where ν is the kinematic viscosity. It will be

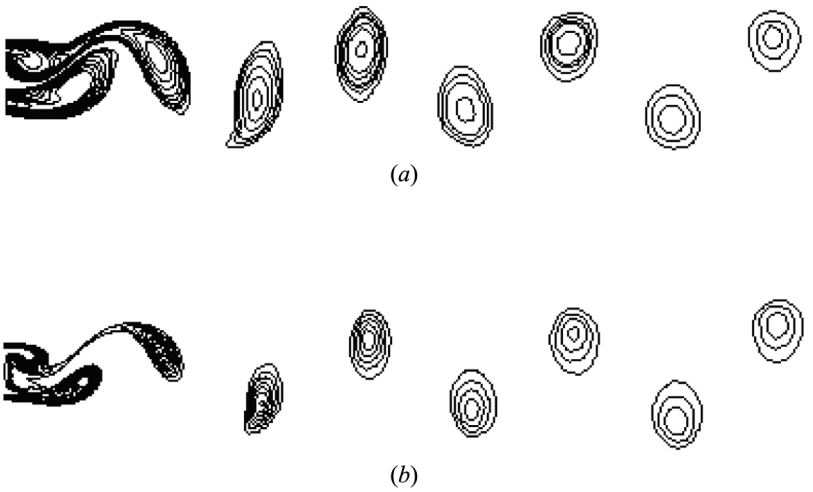

(*a*)

(*b*)

Figure 4. Contours in the downstream wake. (*a*) Vorticity and (*b*) temperature.

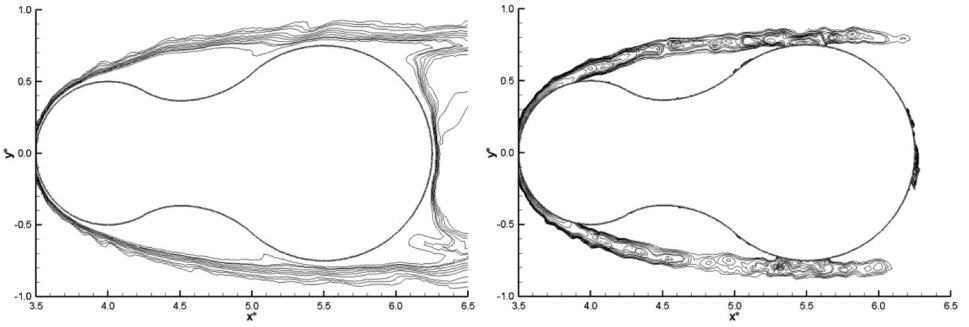

Figure 5. Contours near the wall. (*a*) Temperature and (*b*) vorticity.

observed that only the diffusion coefficient is different from that in the energy equation, so the shape of the two contours is similar. Near the wall, one major difference lies in the fact that the fluctuation in vorticity is more intense than in temperature, as shown in Figures 5*a* and 5*b*, which is mainly due to the fact that the reaction time of the fluid temperature to particle perturbation is longer. Another difference lies in the fact that there be many extreme values in vorticity contour at the center of the closed curve, which is due to the relative motion between the particles and the surrounding fluid.

Figures 6 and 7 show the results simulated separately by single- and two-phase flow models at the same Reynolds number with the corresponding particle volume fractions of 0.2 and 2%. By comparing the computed temperature contours, it can be seen that when the concentration of the particles and the Reynolds number are both very low, the impact of particles on the flow and heat transfer is not significant. For larger numbers of particles, the contour close to the shoulder of the two major arcs has a similar geometry. The sharp increase in the temperature boundary layer is caused mainly by the inertia of particles, and the temperature contours a short

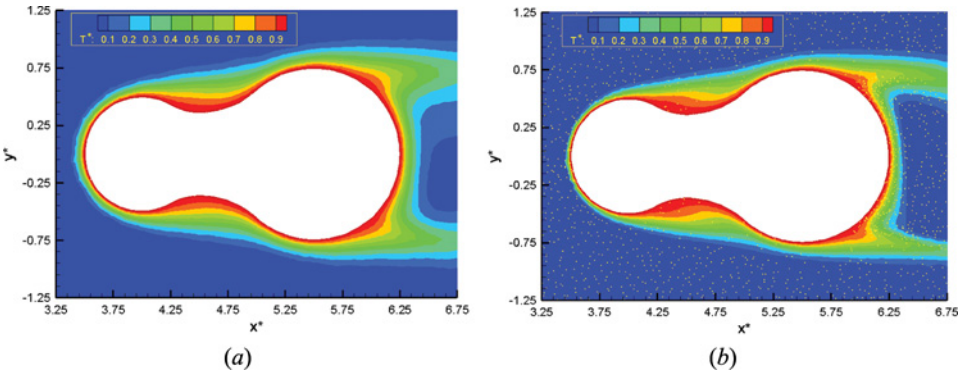

Figure 6. Temperature distribution near the wall. (*a*) Single-phase flow model and (*b*) discrete-phase model.

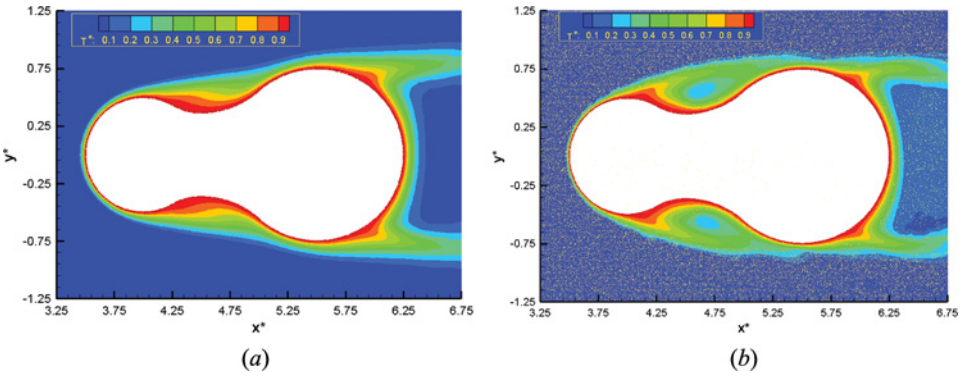

Figure 7. Temperature distribution around the wall. (*a*) Single-phase flow model and (*b*) discrete-phase model.

distance away from the wall exhibit significant waviness, which originates from the impact of particle movement on heat transfer.

The distribution of the vorticity contours near the wall is depicted in Figure 8. As shown by the streamline, two approximately symmetric vortices are found in the waist portion and alternately unsteady vortex shedding in the near wake, which is similar to the flow around a cylinder. Along the wall surface, the locations with zero vorticity indicate the points of flow separation and reattachment corresponding to the semi-saddle points in the streamline. The direction of the tangential velocity

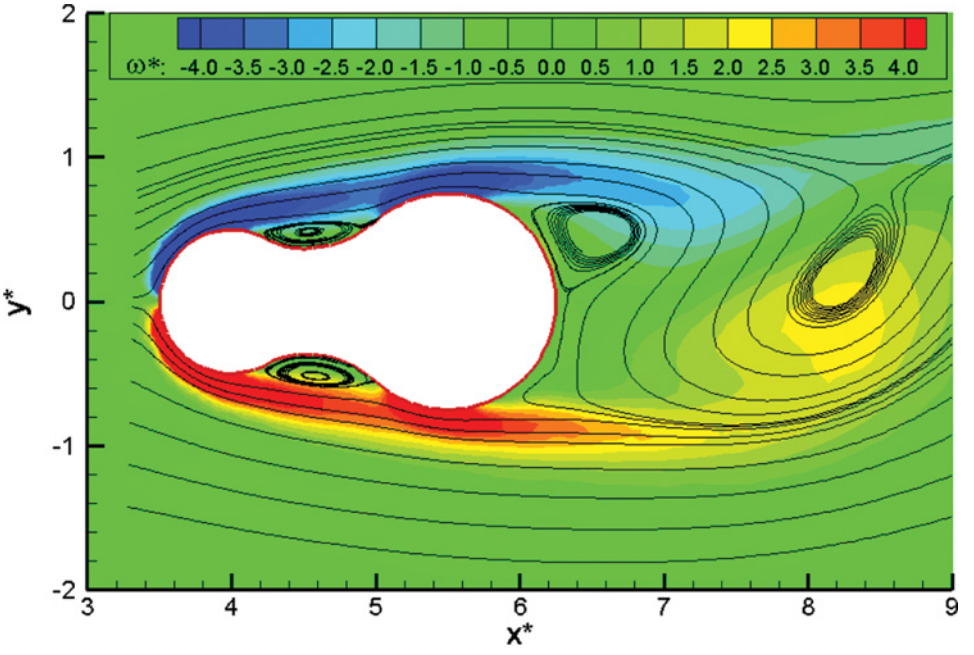

Figure 8. Vorticity and streamline distribution near the wall.

changes in the vicinity of the region. The center of the streamline is different from the position with extreme value in the vorticity. This is due to the fact that the vorticity originates from the boundary and has a greater impact on the vortices near the body.

As shown in Figure 9, when there are no particles in the fluid, the separation point moves forward and the reattachment point moves backward with increased Reynolds number. The vortex in the waist portion becomes larger as the adverse pressure gradient increases, which is similar to the steady wake vortex around the cylinder. The vorticity contour is also depicted in the figure as the background. The zero vorticity line passes through the vortex, and the central line through the center of the vortex can be defined as the vorticity line along which the velocity component equals zero. The angle between the center line and the wall boundary is about two-thirds of that between the separation line and the boundary in the vicinity of the separation point.

Figure 10 shows the temperature distribution and the streamline near the middle portion around the wall at $\mathrm{Re} = 250$. An improved Brown force model is used in the simulation, the particle distribution is more nonuniform than that simulated by the classical model, and the unsteady feature is more obvious. A new drag force model is also adopted in the computation, and the frequency variation in the particle motion is more complex. Particles can be considered as becoming larger in a certain aspect so that the impact of the changes in flow field on particle motion increases compared with the Stokes drag model. Thus, the result simulated here is closer to the actual particle movement in fluid. Comparing the simulation results without nanoparticles, it can be seen that, due to the inertia effect of particles, the streamline is uplifted near the separation point and the separation angle becomes larger, which increases the recirculation zone. The temperature contours deviate with a decrease in the corresponding local Nusselt number, and the inflection point appears in the distribution curve representing small-amplitude fluctuations.

As shown in Figure 11, the initial stage of the particles entering the separated vortex is analyzed. Fluid flow drives the motion of nanoparticles around the

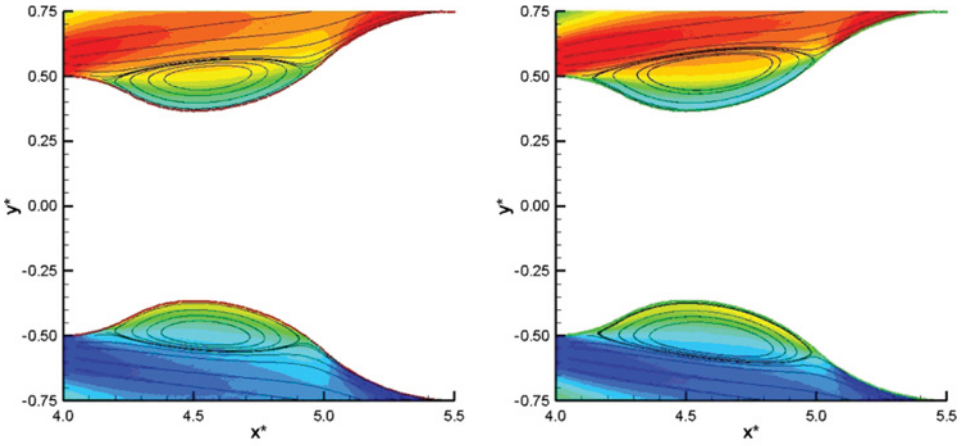

Figure 9. Vorticity distribution and streamline near the waist portion of the calabash-shaped body. (*a*) $\mathrm{Re} = 150$ and (*b*) $\mathrm{Re} = 250$.

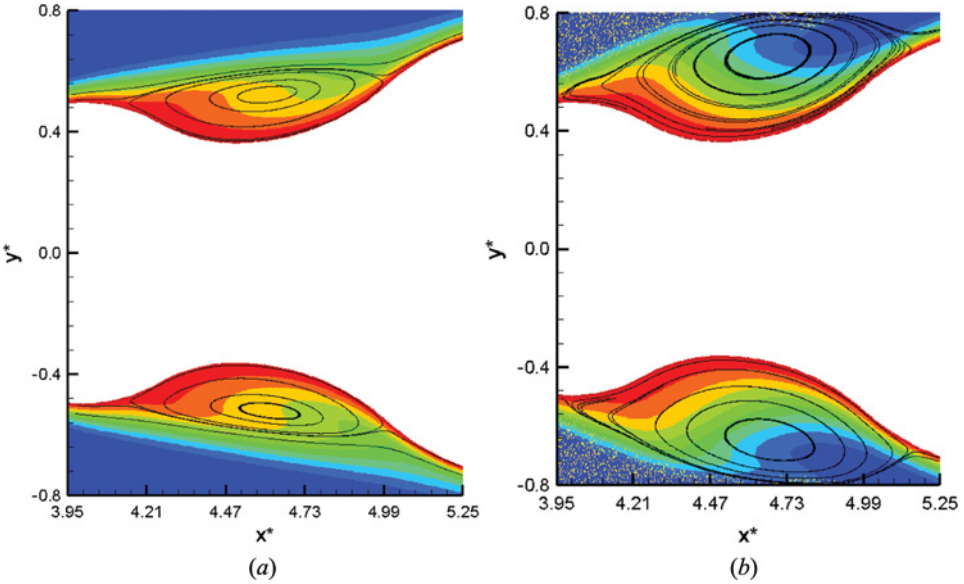

Figure 10. Streamline and temperature distribution near the waist portion of the body. (*a*) Without nanoparticles and (*b*) with nanoparticles.

calabash-shaped body, while the separation movement of particles will in turn affect the development of the vortex. With the development of the nanofluid flow, when the particles pass through the separation point, as shown in Figure 11*a*, the vortex is gradually increased. As the external particles reach $x^* = 5.5$, the separation vortex changes from wide to thin, and the reattachment point shifts toward the downstream direction. After that, few particles move into the separation zone, and the fluid slows down in part of the vortex, which is illustrated in Figure 11*b*. The streamline becomes asymmetric with sparse distribution at the front, which is due to the particles entering the vicinity of the separation point. As depicted in Figure 11*c*, more particles entering the vortex slow the flow development in the recirculation region. As shown in Figure 11*d*, the particles in the separation zone affect the two vortices while those near the outer boundary of the region influence the shape and size of the vortex. The streamline is straighter at the intermediate portion, which will improve the local heat transfer performance of the flow, while the asymmetric features within the vortex are more obvious. Overall, quasi-steady vortex separation undergoes four main stages: it becomes larger, fatter, thinner, and more asymmetric.

If we examine the recirculation zone, at the beginning of the flow no particles appear in the relatively steady vortex. As shown in Figure 12, it can be seen that in the vicinity of the separation point, some particles move in a direction contrary to the movement of the fluid, which is primarily due to the Brownian diffusion effect of particles. Fewer particles move into Region A from the front portion, relatively more particles enter Region B from the reattachment zone, and then they will mix together and move with the swirling vortex.

As shown in Figure 13, the distribution of nanoparticles changes constantly near the trailing edge, which can be generally divided into four stages. Initially

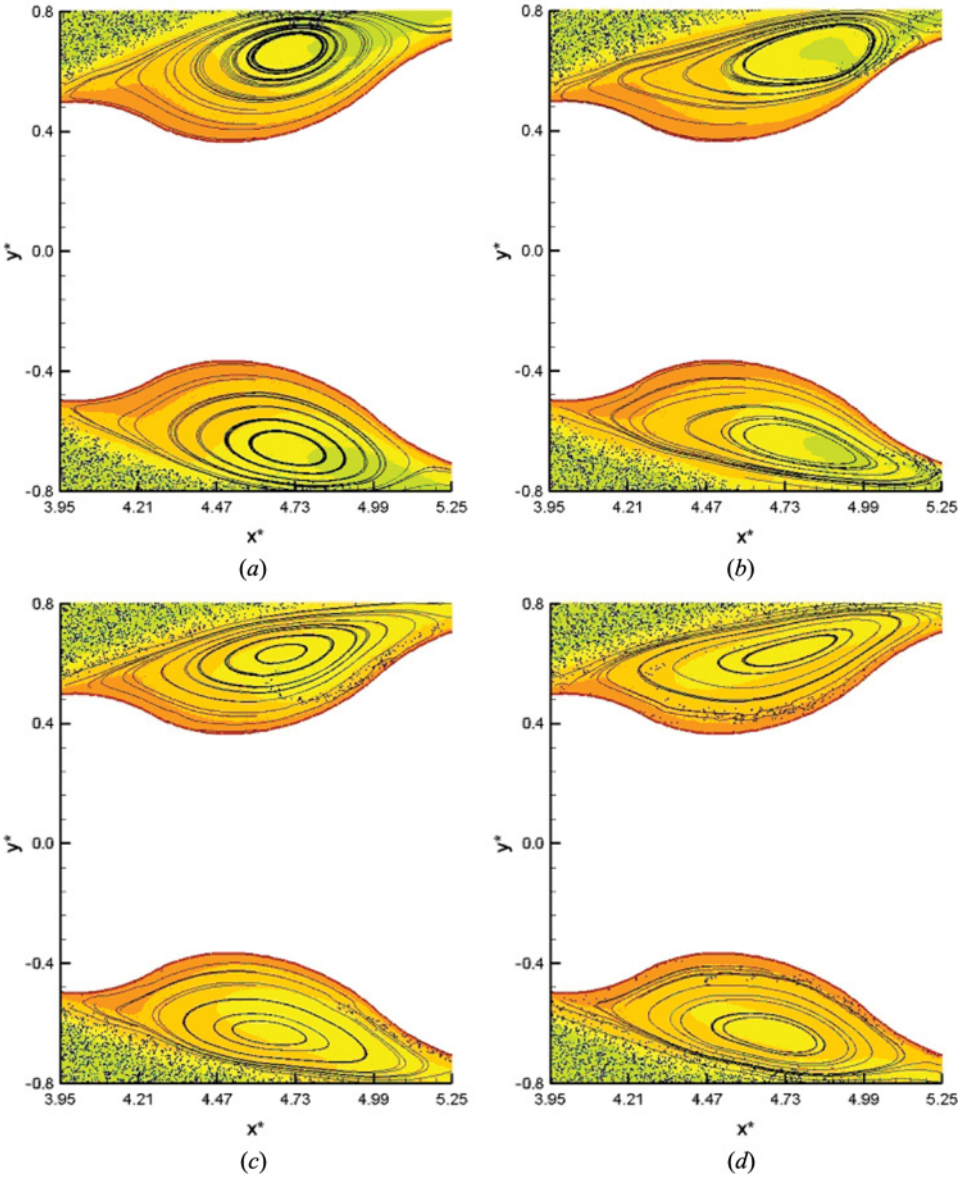

Figure 11. Evolution of particle motion around the separated vortex.

particles move in the same direction with the main flow, then the particles in the upper and lower portions interact with the central shedding vortex in the wake and some move back to the trailing edge, which is shown in Figure 13*a*. Particles migrate to the near wake following the evolution of the upper vortices and appear mainly in the upper portion, while the number of particles moving along the wall is gradually increased, as depicted in Figure 13*b*. Figure 13*c* shows that as the

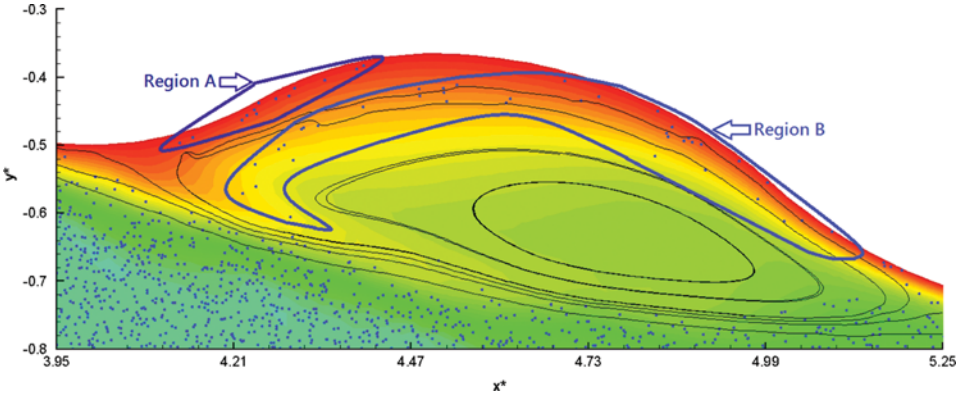

Figure 12. Origin of particles within the quasi-steady separated vortex.

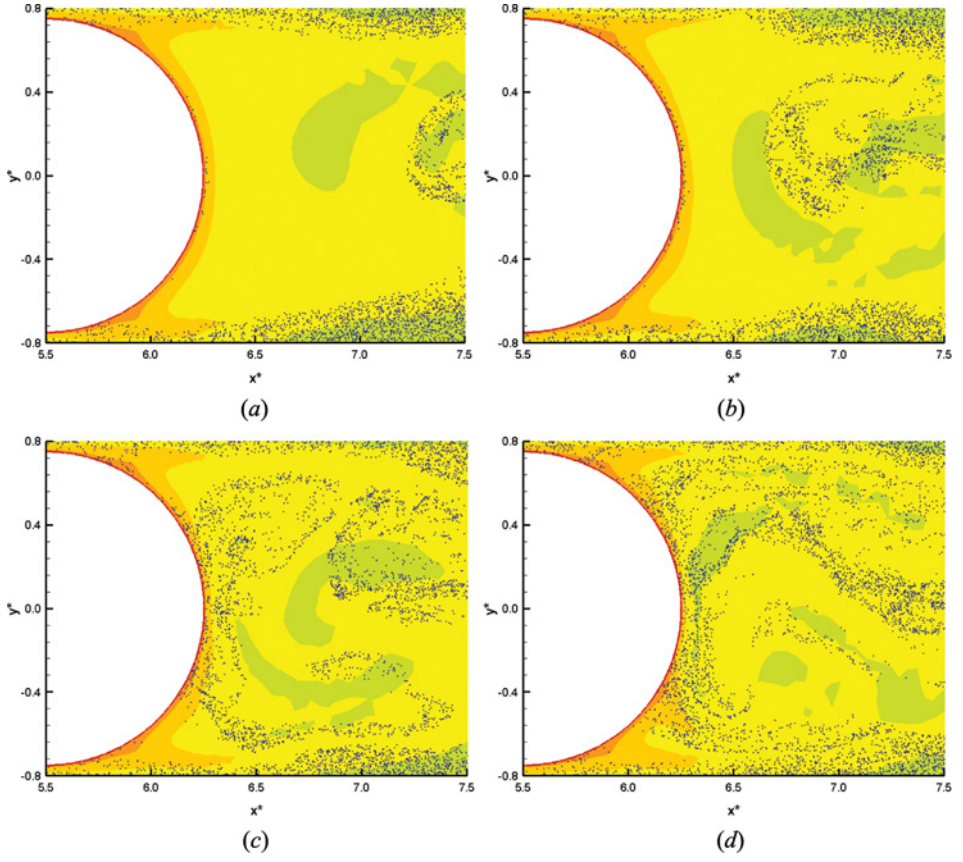

Figure 13. Evolution of particle motion in the near wake.

particles move backward, they collide with the rear of the body and begin to appear in the lower portion of the near wake. When the particles interact fully with the wake around the wall, they virtually cover the trailing edge except near the separation point, as shown in Figure 13*d*. Particles in the unsteady separation zone and the side wake flow start to mix together. The corresponding temperature contours can also be seen in the above figures. Between the first and second stage of the process, the corresponding temperature gradient increases close to the wall, while during the transition from the second to the third stage the gradient decreases slightly near the separation point, resulting from the particles entering the flow velocity more slowly. The enhanced temperature gradient at the trailing edge is primarily due to the increase number of nanoparticles in the final stage.

Figure 14 shows the simultaneous distribution of Nu along the wall for pure water and alumina–water nanofluids. An extreme value of Nusselt number is found in the vicinity of the unsteady rear stagnation point. This decreases gradually along the wall boundary to a minimum value close to the separation point on the larger part of the body. It increases again along the wall up to the reattachment point, then again decreases to a minimum value close to the separation point on the smaller part and increases to its maximum value in the vicinity of the front stagnation point. It can be seen that with increase in particle volume fraction, Nusselt number is increased on the whole as the thermal boundary layer is decreased and the heat transfer performance of flow is improved at higher Reynolds number. For particle volume fraction 4%, as shown in Figure 15, with the development of the flow at $\mathrm{Re} = 150$, some particles move into the recirculation zone. This influences the heat transfer process near the wall and results in a local change in Nusselt number corresponding to an inflection point about $N_b = 100$.

Figure 16 shows that for a small volume fraction of $\varphi < 4\%$, the time-averaged value of Nusselt number increases almost linearly with the volume fraction of nanoparticles. It can be demonstrated that the heat transfer rate is enhanced for nanofluid around this blunt body by the marked increase in both local and average Nusselt number.

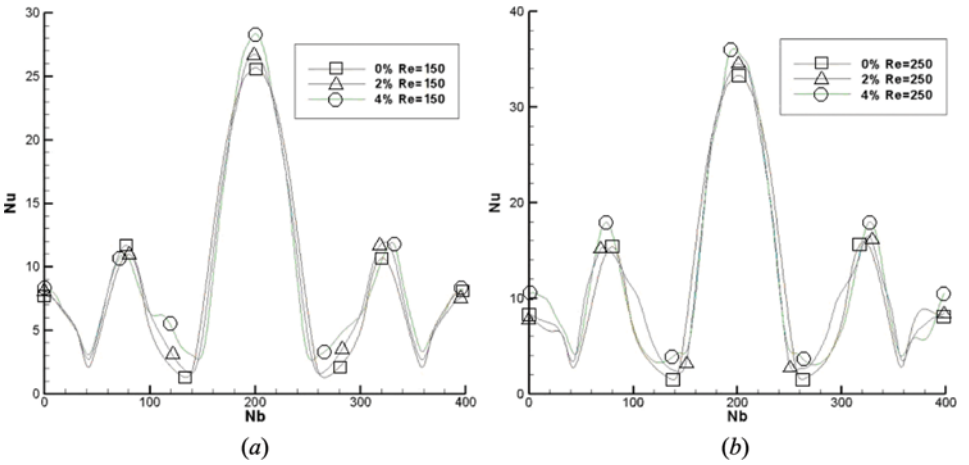

Figure 14. Variation in the Nusselt number along the wall. (*a*) $\mathrm{Re} = 150$ and (*b*) $\mathrm{Re} = 250$.

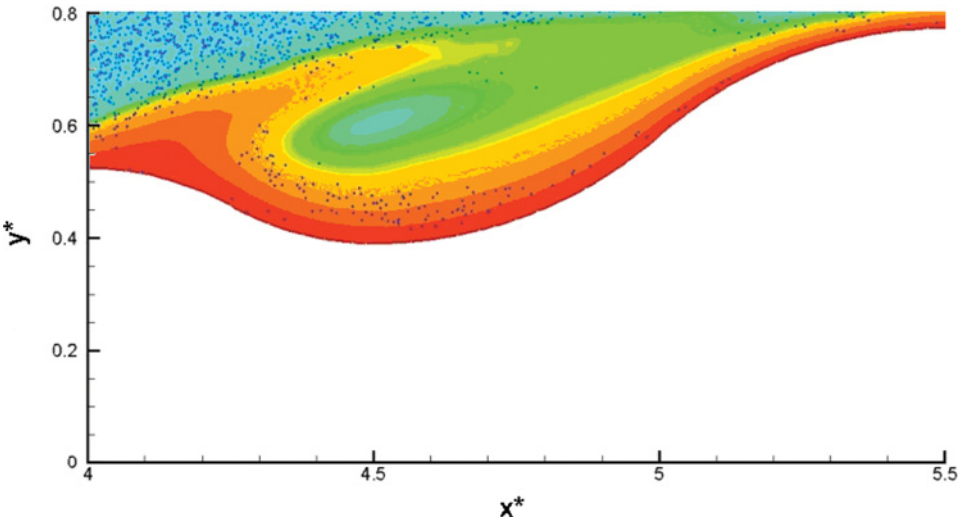

Figure 15. Local distribution of nanoparticles.

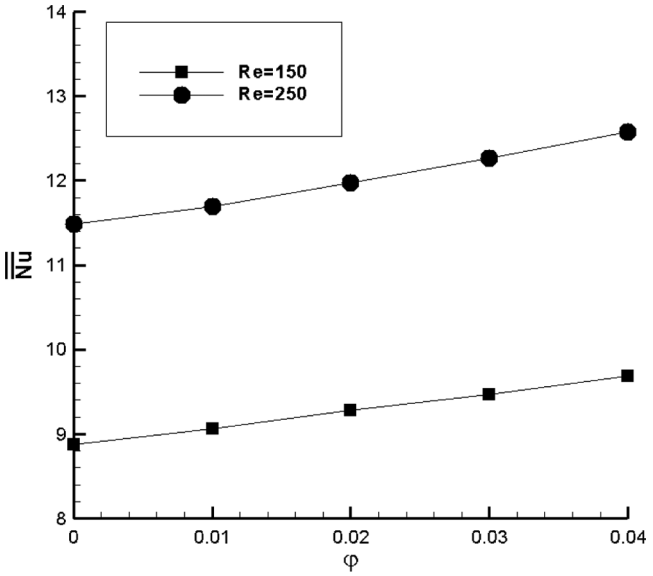

Figure 16. Variation in the average Nusselt number on the wall versus nanoparticle volume fractions.

5. CONCLUSION

Alumina–water nanofluid flow and heat transfer around a calabash-shaped body were numerically investigated by the Euler–Lagrangian method. The major force exerted on particles is calculated using improved models of drag and Brownian force. As the governing equations for vorticity and temperature are expressed in the

same form, the distribution of the two contours shows marked similarity in the downstream wake. Due to particle movement relative to the surrounding fluid, extreme values are found in the vorticity contour around the wall as the center of the closed curve, which is different from those for temperature. For nanofluids with higher particle concentration, the temperature contour close to the shoulder portion of the two major arcs has a similar geometry, with the sharp increase in temperature boundary layer caused by particle inertia. The vortex in the waist portion becomes larger with higher Reynolds number as the adverse pressure gradient increases. Particles in the recirculation region originate mainly from two areas: one near the separation point and the other is the reattachment zone. The temperature gradient increases close to the wall when particles in the near wake move backward and collide with the rear of the body. It is shown that the variation in the Nusselt number relates to the critical points along the wall. The local minimum value corresponds to the separation point in flow, while for the reattachment point and the stagnation point it exhibits a maximum value. The heat transfer characteristics of nanofluids are compared at different volume concentrations. The results show that for unsteady flow around a calabash-shaped body with the addition of nanoparticles, more energy is transported downstream with increased particle volume fraction so that the heat transfer performance is significantly enhanced.

FUNDING

This work was supported by the National Natural Science Foundation of China [Grant Numbers 51406098, 51136001, 51356001, 51322603], the Science Fund for Creative Research Groups [Grant Number 51321002], and the Program for New Century Excellent Talents in University, Tsinghua University Initiative Scientific Research Program, the Tsinghua National Laboratory for Information Science and Technology of China. We also thank the China Postdoctoral Science Foundation [Grant Number 2014M560967].

REFERENCES

1. J. H. Lee, S. H. Lee, C. J. Choi, S. P. Jang, and S. U. S. Choi, A Review of Thermal Conductivity Data, Mechanisms and Models for Nanofluids. *Int. J. Micro–Nano Scale Transport*, vol. 1, pp. 269–322, 2010.
2. J. J. Wang, R. T. Zheng, J. W. Gao, and G. Chen, Heat Conduction Mechanisms in Nanofluids and Suspensions, *Nano Today*, vol. 7, no. 2, pp. 124–136, 2012.
3. O. Mahian, A. Kianifar, S. A. Kalogirou, I. Pop, and S. Wongwises, A Review of the Applications of Nanofluids in Solar Energy, *Int. J. Heat Mass Transfer*, vol. 57, pp. 582–594, 2013.
4. S. K. Das, S. U. S. Choi, and W. H. Yu, *Nanofluids: Science and Technology*, Wiley-Interscience, New York, 2007.
5. G. Donzelli, R. Cerbino, and A. Vailati, Bistable Heat Transfer in a Nanofluid, *Physical Review Letters*, vol. 102, no. 10, pp. 104503, 2009.
6. M. Hejazian and M. K. Moraveji, A Comparative Analysis of Single and Two-Phase Models of Turbulent Convective Heat Transfer in a Tube for TiO_2 Nanofluid with CFD, *Numerical Heat Transfer*, Part A, vol. 63, pp. 795–806, 2013.

7. R. K. Tiwari and M. K. Das, Heat Transfer Augmentation in a Two-Sided Lid-Driven Differentially Heated Square Cavity Utilizing Nanofluids. Int. *J. Heat Mass Transfer*, vol. 50, pp. 2002–2018.
8. B. Ghasemi, and S. M. Aminossadati, Brownian Motion of Nanoparticles in a Triangular Enclosure with Natural Convection, *Int. J. Therm. Sci.*, vol. 49, no. 6, pp. 931–940, 2010.
9. B. Ghasemi, Magnetohydrodynamic Natural Convection of Nanofluids in U-shaped Enclosures, *Numer. Heat Transfer, Part A*, vol. 63, pp. 473–487, 2013.
10. N. Zhang, Z. C. Zheng, and S. Eckels, Study of Heat-Transfer on the Surface of a Circular Cylinder in Flow using an Immersed-Boundary Method, *Int. J. Heat Fluid Flow*, vol. 29, pp. 1558–1566, 2008.
11. M. S. Valipour, and A. S. Ghadi, Numerical Investigation of Fluid Flow, and Heat Transfer Around a Solid Circular Cylinder utilizing Nanofluid, *Int. Commun. Heat Mass Transfer*, vol. 38, pp. 1296–1304, 2011.
12. S. Sarkar, S. Ganguly, and G. Biswas, Mixed Convective Heat Transfer of Nanofluids Past a Circular Cylinder in Cross Flow in Unsteady Regime, *Int. J. Heat Mass Transfer*, Vol. 55, pp. 4783–4799, 2012.
13. V. Etminan-Farooji, E. Ebrahimnia-Bajestan, H. Niazmand, and S. Wongwises, Unconfined Laminar Nanofluid Flow, and Heat Transfer Around a Square Cylinder, *Int. J. Heat Mass Transfer*, Vol. 55, pp. 1475–1485, 2012.
14. S. Kondaraju, E. K. Jin, and J. S. Lee, Effect of the Multi-Sized Nanoparticle Distribution on the Thermal Conductivity of Nanofluids, *Microfluid. Nanofluid.*, vol. 10, no.1, pp. 133–144, 2011.
15. V. Bianco, F. Chiacchio, O. Manca, and S. Nardini, Numerical Investigation of Nanofluids Forced Convection in Circular Tubes, *Appl. Therm. Eng.*, vol. 29, pp. 3632–3642, 2009.
16. E. Abu-Nada, Z. Masoud, and A. Hijazi, Natural Convection Heat Transfer Enhancement in Horizontal Concentric Annuli Using Nanofluids. *Int. Commun. Heat Mass Transfer*, vol. 35, pp. 657–665, 2008.
17. D. S. Wen, L. Zhang, and Y. He, Flow and Migration of Nanoparticle in a Single Channel, *Heat Mass Transfer*, vol. 45, pp. 1061–1067, 2009.
18. S. L. Dong, L. C. Zheng, X. X. Zhang, and P. Lin, Improved Drag Force Model and Its Application in Simulating Nanofluid Flow, *Microfluid. Nanofluid.*, DOI: 10.1007/s10404–014-1330–1, 2014.
19. S. L. Dong, L. C. Zheng, X. X. Zhang, S. P. Wu, and B. Y. Shen, A New Model for Brownian Force and the Application to Simulating Nanofluid Flow, *Microfluid. Nanofluid.*, vol. 16, pp. 131–139, 2014.
20. P. G. Saffman, The Lift on a Small Sphere in a Slow Shear Flow, *J. Fluid Mech.*, vol. 22, pp. 385–400, 1965.
21. S. Kondaraju, E. K. Jin, and J. S. Lee, Investigation of Heat Transfer in Turbulent Nanofluids Using Direct Numerical Simulations, *Phys. Rev. E*, vol. 81, pp. 016304, 2010.
22. O. C. Zienkiewicz, R. L. Taylor, and P. Nithiarasu, *The Finite Element Method for Fluid Dynamics*, 6th edn., Butterworth-Heinemann, London, 2005.
23. A. S. Grove, F. H. Shair, and E. E. Petersen, An Experiment Investigation of the Steady Separated Flow Past a Circular Cylinder. *J. Fluid Mech.*, vol. 19, pp. 60–80, 1964.
24. C. H. K. Williamson, Vortex Dynamics in the Cylinder Wake, *Ann. Rev. Fluid Mech.*, vol. 28, pp. 477–539, 1996.
25. R. H. Khiabani, Y. Joshi, and C. K. Aidun, Heat Transfer in Microchannels with Suspended Solid Particles: Lattice-Boltzmann Based Computations, *J. Heat Transfer*, vol. 132, no. 4, pp. 041003, 2010.
26. S. Mettu, N. Verma, and R. P. Chhabra, Momentum and Heat Transfer from an Asymmetrically Confined Circular Cylinder in a Plane Channel, *Heat Mass Transfer*, vol. 42, no. 11, pp. 1037–1048, 2006.